chapter five

Magnetic properties

Junichiro Kono
Rice University
Stephan Roche
Commissariat à l'Énergie Atomique

Contents

5.1 Introduction

One of the unique properties of carbon nanotubes is that their metallicity can be controlled by an external magnetic field applied parallel to the tube axis. Namely, a carbon nanotube can be either semiconducting or metallic,

depending on the strength of the applied field, and its band gap is predicted to be an oscillatory function of magnetic field with period $\phi_0 = h/e$, i.e., the magnetic flux quantum.[1–9] Thus, metallic tubes can be made semiconducting by applying a (even infinitesimally small) magnetic field parallel to the tube axis, and semiconducting tubes can become metallic in ultrahigh magnetic fields. These exotic magnetic effects are related to the modulation of the electronic wavefunction along the tube circumference by the Aharonov–Bohm phase.[10]

Some of the predictions have been directly verified by a recent interband optical study on single-walled carbon nanotubes (SWNTs).[11] In addition, signatures of novel phenomena, lacking background in conventional theories of mesoscopic transport, seem to have been clearly evidenced in a number of recent magnetotransport studies on carbon nanotubes.[12–19] Indeed, while some studies on large-diameter multiwalled carbon nanotubes (MWNTs) have revealed some signatures of weak localization, with negative magnetoresistance and $\phi_0/2$ periodic Aharonov–Bohm oscillations, other studies have given more importance to the field-modulated band structure effects, assuming a negligible contribution from the quantum interference effects. The possibility of superimposed contributions to the Aharonov–Bohm effect of both band structure and transport phenomena has created a rich and challenging research subject.

In this chapter, we review theoretical and experimental studies on the magnetic properties of carbon nanotubes, including both SWNTs and MWNTs. We first discuss the main effects of an external magnetic field on the electronic properties of carbon nanotubes, with the main focus on how the Aharonov–Bohm phase alters the electronic band structure, density of states, magnetic susceptibility, persistent currents, and magnetotransport properties of carbon nanotubes. A discussion about transport length scales will further elucidate the regimes in which quantum interference effects also affect the transport properties. In the second part, we will describe experimental studies on carbon nanotubes in magnetic fields. In particular, the recent magneto-optical and magnetotransport measurements that have challenged the theoretical predictions will be detailed.

5.2 Theoretical perspectives

5.2.1 Band structure in magnetic fields

The electronic spectrum of metallic or semiconducting carbon nanotubes is characterized by a set of van Hove singularities (VHSs) that reflects the quantized momentum component along the circumferential direction. Their precise locations can be analytically derived from the dispersion relations. As an illustration, if we consider armchair metallic tubes with helicity (N,N) and restrict ourselves to the π and π^* bands, the dispersions are given by

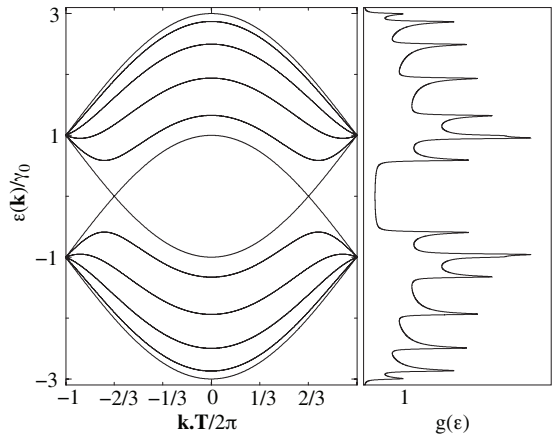

Figure 5.1 Dispersion relations and density of states for the (5, 5) metallic nanotube.

$$E_q^{\pm}\left(k\right) = \pm\gamma_0\sqrt{1 \pm 4\cos\frac{ka}{2}\cos\frac{q\pi}{N} + 4\cos^2\frac{ka}{2}}\ , \tag{5.1}$$

where $q(= 1, 2,\ldots, 2N)$ specifies the discrete part of the wavevector perpendicular to the tube axis (i.e., the band index), while k is the continuous component that describes eigentates in a given subband ($-\pi < ka < \pi$); a = 2.46 Å and $\gamma_0 \sim 2.7$ eV. The dispersion relations of the (5, 5) tube and the (10, 0) zigzag tube are shown in Figure 5.1 and Figure 5.2, respectively, together with the corresponding densities of states (DoSs), $g(\varepsilon)$. The VHS positions are derived from the condition $\partial E_q(k)/\partial k = 0$, which, for the armchair tubes, yields $\varepsilon_q = \pm\ \gamma_0 \sin(q\pi/N)$.

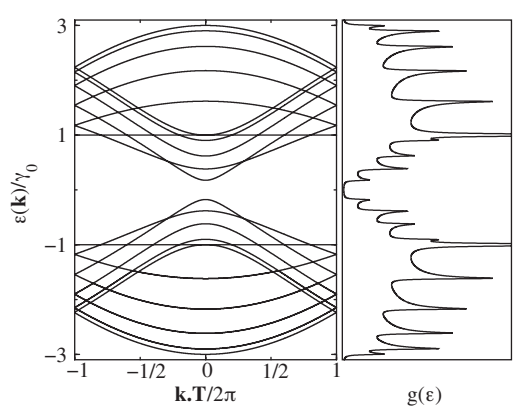

Figure 5.2 Dispersion relations and density of states for the (10, 0) semiconducting nanotube.

5.2.1.1 Parallel field: the Aharonov–Bohm effect

Given the specific electronic structure of a carbon nanotube, it is relatively straightforward to show that the application of an external magnetic field modifies the band structure in a truly unique manner. When applied parallel to the tube axis, the magnetic field has a direct impact on the phase of the corresponding electronic wavefunctions, under the Aharonov–Bohm effect. As a consequence, all the VHSs shift either upward or downward in energy, resulting in an apparent VHS splitting. An intriguing consequence is the opening of an energy gap in a metallic tube, which oscillates with magnetic field. A magnetic field can thus transform a metallic system into a semiconducting one and vice versa.[1,5–7]

More precisely, in the presence of a magnetic field, the modifications of wavefunction quantum phases are determined by the vector potential $\vec{A}$. Within the basis $\{C_h / |C_h|,\ T / |T|\}$ defined by the helical vector C_h and the unit cell vector $\vec{T}$ of the nanotube,[20] the vector potential in the Landau gauge reads $\vec{A} = (\phi / |C_h|, 0)$ (ϕ is the magnetic flux through the tube cross section). The phase factor appears in the electronic coupling factors between site $r = (x, y)$ and $r' = (x', y')$ and can be written as[1,5–7,20], $\Delta\varphi_{r,r'} = \int_0^1 (r' - r) \cdot (A(r + \lambda[r' - r]))d\lambda$, so that $\Delta\varphi_{r,r'} = i(x - x')\phi / |C_h|$. This yields a new expression for the quantization relation of the corresponding wavevector component $\delta k(\phi) \cdot \kappa_\perp = \delta k(0) \cdot \kappa_\perp + 2\pi\phi / (\phi_0 |C_h|)$, with $\kappa_\perp$, the unit vector of reciprocal space, associated with C_h. Such modulation in turn will shift the VHS positions, as illustrated in Figure 5.3.

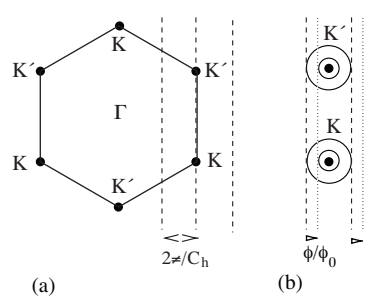

Figure 5.3 (a) Representation of the first Brillouin zone of a graphene sheet together with allowed states for an armchair tube (dashed lines) at zero flux. (b) Modifications of allowed states in the vicinity of $\vec{K}$-points, under the effect of a magnetic field applied parallel to the tube axis (circles give the equipotentials close to the Fermi energy).

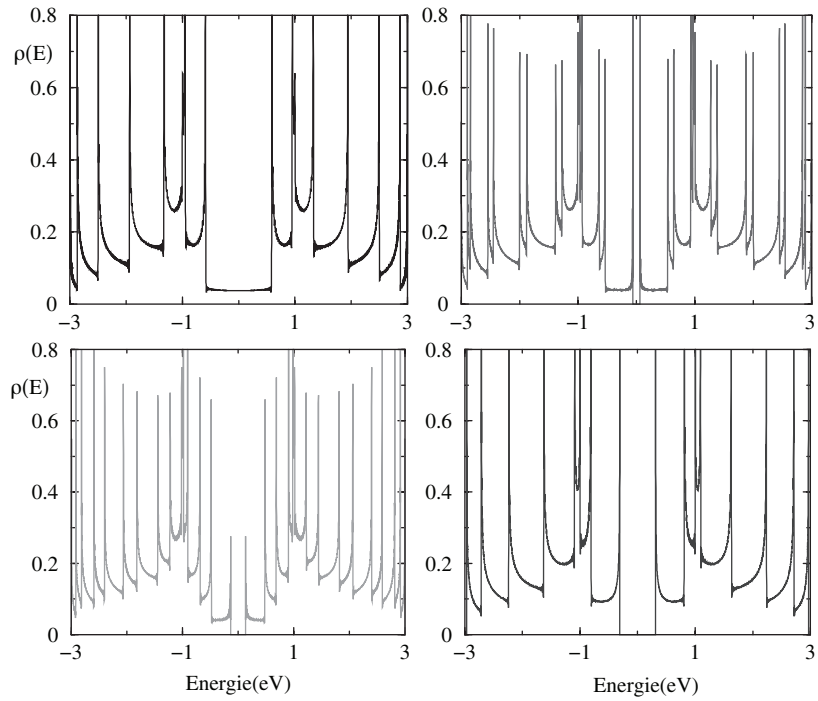

Figure 5.4 Density of states of the (5, 5) carbon nanotube for several magnetic flux values: $\phi/\phi_0 = 0$ (black curve), $\phi/\phi_0 = 0.1$ (red curve), $\phi/\phi_0 = 0.2$ (green curve), and $\phi/\phi_0 = 0.5$ (blue curve). This is a metallic tube at zero magnetic flux, but a gap opens up once a finite flux is applied, and it increases with the flux. The calculations were performed following the algorithm established in Roche.[21]

The magnetic flux thus modulates the band structure in a ϕ_0-periodic fashion, with a band gap opening and closing. Such phenomenona are illustrated in the DoS plots for the (5, 5) tube and (10, 10) tube in Figure 5.4 and Figure 5.5, respectively. Note that both tubes are metallic at zero magnetic field, but a band gap opens up once a finite magnetic flux ϕ threads the tube, and the induced band gap increases linearly with ϕ, and reaches a maximum value at half quantum flux. The traces (a) to (e) in Figure 5.5 are the DoSs for the (10, 10) tube at ϕ/ϕ_0 = (a) 0, (b) 0.125, (c) 0.25, (d) 0.375, and (e) 0.5. For $\phi/\phi_0 = 0.125$ (trace (b)), one notices that in the vicinity of the charge neutrality point (i.e., $\varepsilon = 0$), a new VHS appears, indicating the gap opening. In traces (c) to (e), the gap is seen to increase and reach its maximum value at $\phi/\phi_0 = 0.5$. The evolution of VHSs is then reversed and the gap closes again at $\phi/\phi_0 = 1$. For VHSs at higher energies (e.g., that located at $\varepsilon_{q=1}$), the oscillatory behavior is slightly more involved: at low fields a splitting is observed for each VHS, which is followed by crossing at higher flux, and finally all the VHSs return to the orginal positions when $\phi/\phi_0 = 1$ (see the inset of Figure 5.5).

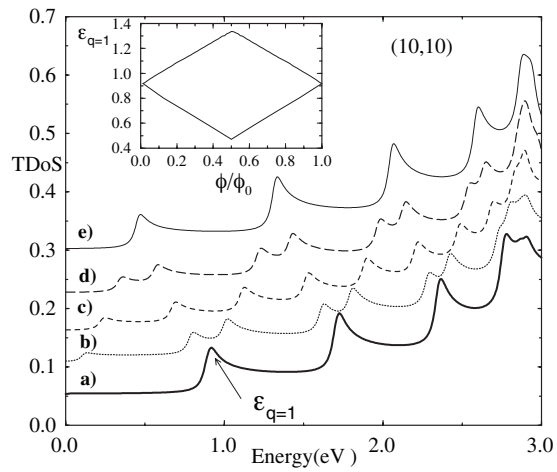

Figure 5.5 Density of states of the (10, 10) metallic tube as a function of energy for several magnetic flux values (see text). The curves have been vertically offset for clarity. Inset: Evolution of one VHS with magnetic flux.

An analytic expression for the gap evolution for (n, m) tubes with $n - m = 3M$ (M: = integer) can be derived easily as

$$\Delta_g = \begin{cases} 3\Delta_0 \dfrac{\phi}{\phi_0} & \text{if} \quad 0 \le \phi \le \dfrac{\phi_0}{2}, \\ 3\Delta_0 \left| 1 - \dfrac{\phi}{\phi_0} \right| & \text{if} \quad \dfrac{\phi_0}{2} \le \phi \le \phi_0, \end{cases} \tag{5.2}$$

where $\Delta_0 = 2\pi a_{cc}\gamma_0 / |\, C_h \,|$ and $a_{cc} = 1.421$ Å. Numerically, $\Delta_g \approx 75$ meV at 50 T for the (22, 22) tube (diameter ≈ 3 nm). The van Hove singularity splitting, which can be investigated by spectroscopic experiments (cf. Section 5.2), can be also derived analytically. For instance, in the case of armchair tubes, the magnitude of the field-dependent splitting of the q-th VHS is given by

$$\Delta_B\left(\varepsilon_q, \phi/\phi_0\right) = 2\gamma_0 \left[\sin\frac{\pi}{q}\left(\cos\frac{\pi\phi}{q\phi_0} - 1 \right) - \cos\frac{\pi}{q} \sin\frac{\pi\phi}{q\phi_0} \right] \tag{5.3}$$

For instance, $\Delta_B \approx 40$ meV at 60 T for the (10, 10) tube (diameter = 1.4 nm). In this parallel configuration, let us note that to obtain a field equivalent to $\phi = \phi_0$ in nanotubes with diameters of 1, 10, 20, and 40 nm, one would need magnetic fields of 5325, 53, 13, and 3 T, respectively.

Semiconducting tubes (i.e., (n, m) tubes with $n - m = 3M \pm 1$ (M: integer)] are affected in a similar way, but the gap expression is slightly different:

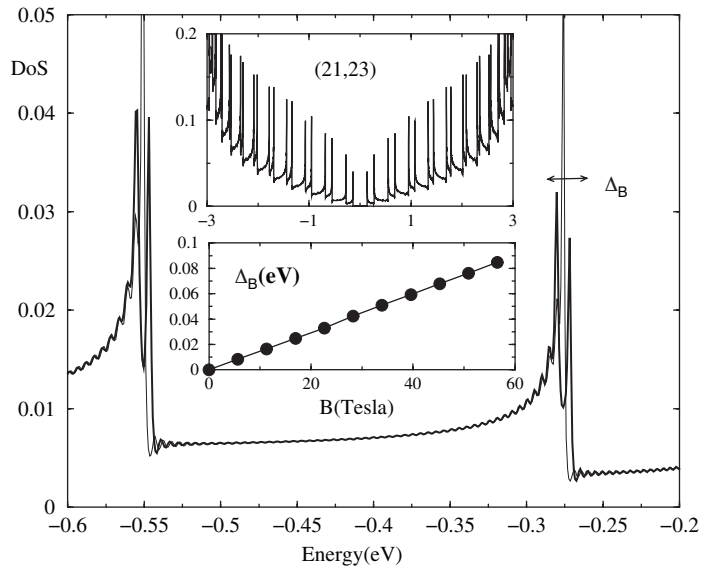

Figure 5.6 Density of states of the (21, 23) tube at zero and finite flux. Top inset: Expanded plot of the DoS. Bottom inset: Evolution of the VHS splitting Δ_B as a function of magnetic field.

$$\Delta_g = \begin{cases} \Delta_0 \left| 1 - \dfrac{3\phi}{\phi_0} \right| & \text{if} \quad 0 \le \phi \le \dfrac{\phi_0}{2}, \\ \Delta_0 \left| 2 - \dfrac{3\phi}{\phi_0} \right| & \text{if} \quad \dfrac{\phi_0}{2} \le \phi \le \phi_0. \end{cases} \tag{5.4}$$

Thus, the energy gap, which is Δ_0 at zero field, continuously decreases with increasing ϕ and becomes zero at $\phi = \phi_0/3$, at which magnetic field the tube is metallic. The gap then changes in an intriguing way as ϕ increases from $\phi_0/3$, reaching a local maximum ($\Delta_0/2$) at $\phi = \phi_0/2$, becoming zero again at $\phi = 2\phi_0/3$, and finally recovering Δ_0 at $\phi = \phi_0$. In Figure 5.6, we show the case of a 3-nm-diameter semiconducting single-walled tube.

5.2.1.2 Perpendicular field: Landau quantization

The application of a magnetic field perpendicular to the tube axis leads to completely different effects. In this configuration, the zero-field band structure with characeristic one-dimensional VHSs is gradually modified into a Landau-level spectrum as the field increases. The relevant dimensionless parameter that allows us to quantify the appearance of Landau levels is given by $\nu = |C_h| 2\pi\ell_m$, where $_m = \sqrt{\ /eB}$ is the magnetic length (first cyclotron orbit radius). The vector potential A within the Landau gauge is

now given by $A = \left(0, \frac{|C_h|B}{2\pi}\sin\left(\frac{2\pi x}{|C_h|}\right)\right)$ in the basis $\{ C_h / | C_h |, T / | T |$. Seri and Ando have demonstrated that close to the K-points the electronic eigenstates can be analytically written as[22,23]

$$\Psi_{nsk}(r) = \frac{1}{\sqrt{2L_{tube}}}\begin{pmatrix} \pm is\Psi-(x) \\ \Psi+(x) \end{pmatrix} e^{iky}, \tag{5.5}$$

$$\Psi\pm(x) = \frac{1}{\sqrt{|C_h| I_0(2\nu^2)}} e^{\pm\nu^2\cos\left(\frac{2\pi x}{C_h}\right)}, \tag{5.6}$$

where $I_0(2\nu^2)$ is the modified Bessel function of the first kind. One can also find the dispersion relation and the DoS in the vicinity of the Fermi level (charge neutrality point) as $E^{\pm}_{q=0} = \pm\gamma_0 |k| / I_0(2\nu^2)$ and $\rho(E_F) \sim \frac{I_0(2\nu^2)}{\pi\gamma_0} \sim \frac{e^{\nu^2}}{\sqrt{4\pi\nu^2}}$ ($\nu >> 0$), respectively. As a result, the DoS at the charge neutrality point diverges exponentially with increasing magnetic field. This effect is shown in Figure 5.7 for the (10, 10) tube for several magnetic field strengths. The remaining part of the DoS (VHSs) also progressively degrades as the Landau-level structure starts dominating the spectrum. Given the obvious scaling properties, the larger the tube diameter, the smaller the value of the magnetic field required to form and observe Landau levels.

As soon as $\nu = | C_h | / 2\pi\ell_m \leq 1$ is satisfied, the DoS spectrum is totally dominated by Landau levels. One finds that for tubes with diameters of 1, 10, 20, and 40 nm, the condition $\nu = 1$ corresponds to magnetic field strengths of 2635, 26, 6.6, and 1.6 T, respectively. In each case, $\ell_m \ll \ell_m$ (or $w_c\tau_e \gg 1$) has to be further satisfied for clear observation of Landau quantization, where ℓ_e is the mean free path, $w_c = eB/m$ is the cyclotron frequency, and τ_e is the scattering time (this condition is easily met at such high magnetic fields in carbon nanotubes since ℓ_e can be as long as 1 μm). Such Landau-level formation was first reported by Kanda et al.[15]

5.2.2 *Magnetic susceptibilities*

The strong magnetic field dependence of the band structure suggests a large orbital magnetic susceptibility, χ. Calculations demonstrate that the orbital component of χ is indeed several orders of magnitude larger than the paramagnetic (or Pauli) contribution due to the electron spin.[4,24–27] At zero temperature, the orbital part of χ can be computed from the second derivative of the free energy, which is in turn related to the band dispersion, i.e.,

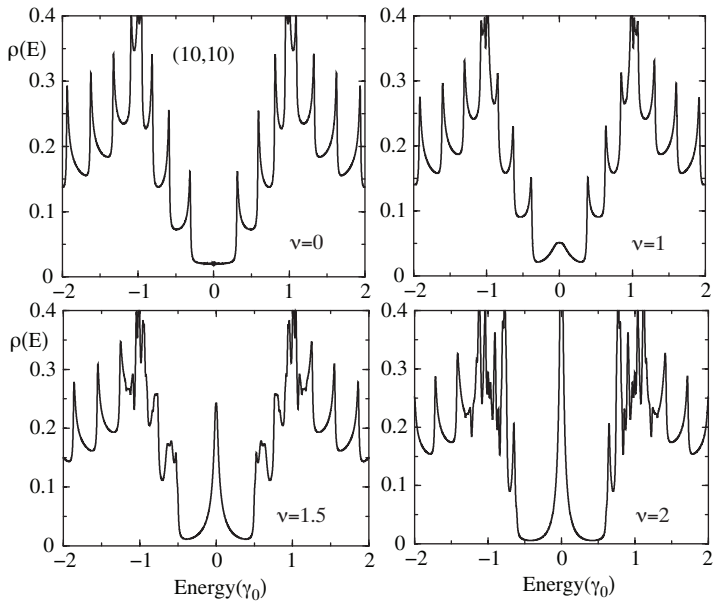

Figure 5.7 Density of states of the (10, 10) tube in a perpendicular magnetic field for several field strengths. The field strengths are expressed in terms of the dimensionless parameter $\nu = |\vec{C}_h|/2\pi\ell_m$, where $\ell_m = \sqrt{\ /eB}$ is the magnetic length.

$$\chi = k_B T \frac{\partial^2}{\partial B^2} \sum_{nk} \ln\left[1 + \exp\left(-\frac{\varepsilon_n(k,\phi) - \mu}{k_B T}\right)\right] \tag{5.7}$$

Calculations have been performed for isolated single-walled carbon nanotubes[4,24,25] as well as for ensembles (bundles) of nanotubes,[27] in which averaging occurs in conjunction with the effect of intertube coupling on individual signatures.

AU: Please double-check, as Figure 5.8 was listed twice here.

An interesting aspect concerns the magnetic anisotropy, i.e., difference between $\chi_\parallel$ and $\chi_\perp$, which can be computed for magnetic fields parallel or perpendicular to the tube axis (Figure 5.8). It is found theoretically that for undoped metallic tubes (for which the Fermi energy is exactly at the charge neutrality point), $\chi_\parallel$ is positive (paramagnetic), whereas $\chi_\perp$ is negative (diamagnetic); $\chi_\parallel$ rapidly decreases as the Fermi energy deviates from the charge neutrality point, exhibiting logarithmic divergence, while $\chi_\perp$ remains almost constant as a function of Fermi energy near the charge neutrality point (Figure 5.8b and c). For undoped semiconducting tubes, both $\chi_\parallel$ and $\chi_\perp$ are negative (diamagnetic) and $|\chi_\perp| > |\chi_\parallel|$ (Figure 5.9). As the Fermi energy is varied in a semiconducting tube, both $\chi_\parallel$ and $\chi_\perp$ remain constant as long as the Fermi energy lies within the band gap; however, square root-like divergence appears in $\chi_\parallel$ when the Fermi energy enters the band edges, as shown

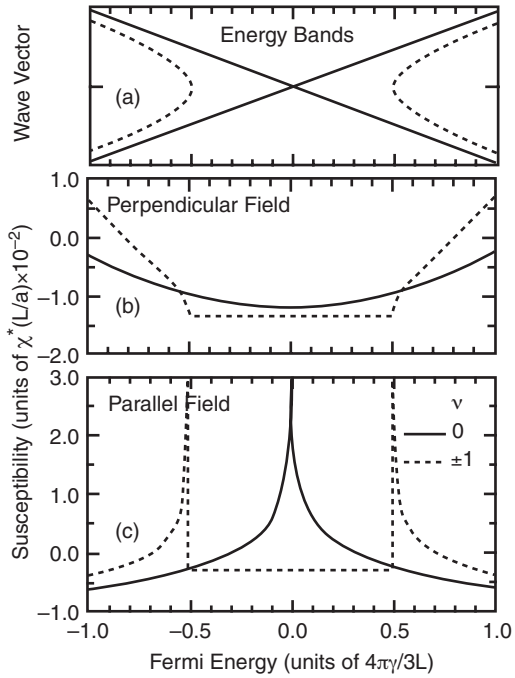

Figure 5.8 The (a) band structure, (b) $\chi_{\perp}$, and (c) $\chi_{\parallel}$ of metallic (solid lines) and semiconducting (dashed lines) SWNTs calculated by Ajiki and Ando. (Adopted from H. Ajiki and T. Ando, *J. Phys. Soc. Jpn.*, 64, 4382, 1995.)

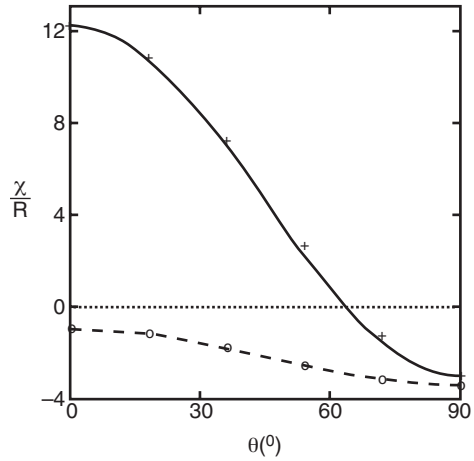

Figure 5.9 The scaled magnetic susceptibility as a function of the angle between the tube and axis and the applied magnetic field for metallic (pluses and dotted line) and semiconducting (diamonds and dashed line) SWNTs calculated by Lu. *R* is the tube diameter. (Adopted from J. P. Lu, *Phys. Rev. Lett.*, 74, 1123, 1995.)

in Figure 5.8c. In contrast, $\chi_\perp$ does not exhibit any divergence and is diamagnetic around the charge neutrality point region for both metallic and semiconducting tubes. In all cases, the susceptibility increases linearly with the tube radius, which makes it possible to define universal relations for $\chi_\perp$ and $\chi_\parallel$. With increasing temperature, $\chi_\parallel$ is predicted to decrease (increase) for metallic (semiconducting) tubes, while $\chi_\perp$ is predicted to increase for both metallic and semiconducting nanotubes.[27] Experimental studies of magnetic susceptibilities are discussed in Section 5.3.1.

Recent experiments[16] have demonstrated that states near the energy gap have a magnetic moment much larger than the Bohr magneton — results that confirm that the electronic motion around the tube circumference plays an important role in the magnetic susceptibility.

5.2.3 *Magnetotransport phenomena*

5.2.3.1 *Fermi's golden rule and mean free path*

Disorder in carbon nanotubes may come from several different origins — chemical impurities, topological defects, Stone–Wales, and vacancies. These lattice imperfections induce departure from ballistic transport, and yet preserve quantum interference effects, which can be profoundly affected by magnetic fields. Unlike strictly one-dimensional systems, disorder effects in nanotubes are strongly energy dependent, as pointed out in early theoretical studies[1,5–7,28–30] and recently confirmed for chemically doped (boron and nitrogen) nanotubes.[31] A crucial transport length scale is the so-called elastic mean free path ℓ_e, i.e., the free propagation length of coherent wavepackets before a collision occurs on the defect, an event that alters momentum without changing the energy of incident electrons.

Within Fermi's golden rule (FGR), the scattering time τ as well as the mean free path $\ell_e = \upsilon_F\tau$ can be analytically derived. FGR writes

$$\frac{1}{2\tau_e\left(E_F\right)} = \frac{2\pi}{}\left|\left\langle \Psi_{n1}\left(k_F\right)\middle|\hat{U}\middle|\Psi_{n2}\left(-k_F\right)\right\rangle\right|^2 \rho\left(E_F\right)\times N_c N_{Ring} \tag{5.8}$$

where N_c and N_{Ring} are the numbers of atomic pairs along the circumference and the total number of crowns within a unit cell (case of armchair tubes), respectively, whereas $\hat{U}$ is the potential describing the elastic collision processes, and the DoS per carbon atom at the charge neutrality point $\rho\left(E_F\right) = \frac{2\sqrt{3}a_{cc}}{\pi\gamma_0|C_h|}$.[32] Thus, rewriting the eigenstates as

$$\left|\Psi_{n1,n2}\left(k_F\right)\right\rangle = \frac{1}{\sqrt{N_{Ring}}}\sum_{m=1,N_{Ring}} e^{imk_F}\left|\alpha_{n1,n2}\left(m\right)\right\rangle \tag{5.9}$$

with

$$\left|\alpha_{n1}(m)\right\rangle = \frac{1}{\sqrt{2N_c}} \sum_{n=1}^{N_c} e^{\frac{2i\pi m}{N_c}} \left(\left|p_\perp^A(mn)\right\rangle + \left|p_\perp^B(mn)\right\rangle\right) \tag{5.10}$$

$$\left|\alpha_{n2}(m)\right\rangle = \frac{1}{\sqrt{2N_c}} \sum_{n=1}^{N_c} e^{\frac{2i\pi m}{N_c}} \left(\left|p_\perp^A(mn)\right\rangle - \left|p_\perp^B(mn)\right\rangle\right) \tag{5.11}$$

and taking as an effective disorder model the so-called Anderson-type disorder with white noise statistics, i.e.,

$$\left\langle p_\perp^A(mn)\middle|\hat{U}\middle|p_\perp^A(m'n')\right\rangle = \varepsilon_A(m,n)\delta_{mm'}\delta_{nn'} \tag{5.12}$$

$$\left\langle p_\perp^B(mn)\middle|\hat{U}\middle|p_\perp^b(m'n')\right\rangle = \varepsilon_B(m,n)\delta_{mm'}\delta_{nn'} \tag{5.13}$$

$$\left\langle p_\perp^A(mn)\middle|\hat{U}\middle|p_\perp^A(m'n')\right\rangle = 0 \tag{5.14}$$

where $\varepsilon_B(m, n)$ and $\varepsilon_A(m, n)$ are the site energies on π-orbitals located on A and B atoms, that are taken at random within $[-W/2, W/2]$ (probability density $\mathscr{P} = 1/W$), one then finally gets

$$\frac{1}{2\tau_e(E_F)} = \frac{2\pi}{4}\frac{1}{}\left(\frac{1}{\sqrt{N_c N_{Ring}}}\sum_{N_c N_{Ring}} \varepsilon_A^2 + \frac{1}{\sqrt{N_c N_{Ring}}}\sum_{N_c N_{Ring}} \varepsilon_B^2\right)\rho(E_F)\ . \tag{5.15}$$

Hence, an analytical expression for the mean free path is[7,28]

$$_e = \frac{18 a_{cc}\gamma_0^2}{W^2}\sqrt{n^2 + m^2 + nm}\ . \tag{5.16}$$

The mean free path thus increases with diameter at fixed disorder, a property that is totally unconventional for usual mesoscopic systems. For a metallic tube (5, 5) with $W = 0.2$, $\ell_e \sim 500$ nm, which turns out to be larger than the circumference. Numerical results obtained via an order N computational approach have confirmed some specific scaling law for ℓ_e that restricts to some interval around the charge neutrality point, which decreases with increasing diameter. The dependence of ℓ_e on the Fermi

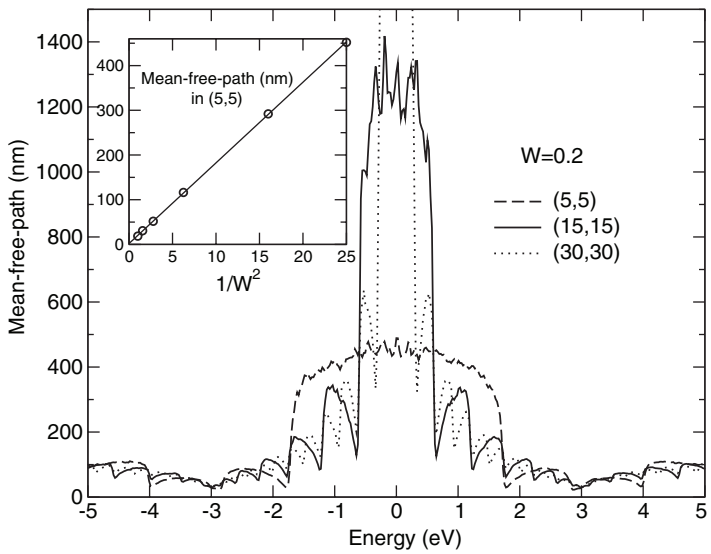

Figure 5.10 Energy-dependent mean free paths for metallic armchair nanotubes with varying diameters. Inset: $1/W^2$ law in agreement with FGR.[33]

energy and $1/W^2$ is illustrated for three armchair tubes with different diameters in Figure 1.10.[33] As soon as the Fermi level is upshifted/downshifted out of the vicinity of the charge neutrality point, the $1/\ell_e$ law is invalidated while the $1/W^2$ law remains applicable. It is interesting to note that these properties remain valid for more realistic disorder as demonstrated in Latil et al.[31] for nitrogen or boron-doped metallic tubes, in full agreement with experimental estimates.[34,35]

5.2.3.2 *Aharonov–Bohm phenomena: ballistic vs. diffusive regimes*

Applying a magnetic field is a powerful tool for unveiling quantum interference effects. In the presence of elastic disorder, the weak localization scheme can be illustrated for metallic nanotubes. The magnetoresistance depends on the probability $\mathcal{P}$ for an electronic wavepacket to go from one site $|P\rangle$ to another $|Q\rangle$, which can be written as

$$\mathcal{P}_{|P\rangle\to|Q\rangle} = \sum_i \left|\mathcal{A}_i\right|^2 + \sum_{i\neq j} \mathcal{A}_i \mathcal{A}_j e^{i(\alpha_i-\alpha_j)} \tag{5.17}$$

where $\mathcal{A}_i e^{i\alpha_i}$ is the probability amplitude to go from $|P\rangle$ to $|Q\rangle$ via the i-path. Most of the terms in the summation vanish when averaged over disorder. In the special case of a cylinder or a nanotube, two paths returning back to the origin yield constructive contribution of quantum interference, reducing the conductance (weak localization). Switching on a magnetic field jeopardizes the

time-reversal symmetry of these paths, resulting in an increase of conductance or decrease of resistance (negative magnetoresistance).

Another magnetic field-induced quantum interference effect in a ring or cylinder geometry is the modulation of resistance with period $\phi_0/2$. The phase factor can then be written as (A = the vector potential)

$$\alpha_{\pm} = \pm \frac{e}{c} \int A.\mathrm{d}r = \pm \frac{2\pi}{\phi_0} \int A.\mathrm{d}r \ , \tag{5.18}$$

and so the amplitude is given by $|\mathcal{A}|^2 \ |1 + e^{i(\alpha_+ - \alpha_-)}|^2$, resulting in a modulation factor $\cos(2\pi\phi/\phi_0)$. Below, the behaviors of field-dependent diffusion coefficients are shown for the (9, 0) nanotube as a function of mean free path evaluated through analytical formulas.[36,37] By using the Anderson-type disorder, the value of the mean free path can be tuned by the disorder strength W, so that several situations of interest can be explored.

First, the weak localization regime[38] is analyzed under the condition $\ell_e < |C_h| < L(\tau_\phi)$. Figure 5.11 shows that the diffusivity increases at low fields (negative magnetoresistance) and that the periodic Aharonov–Bohm oscillations are dominated by a $\phi_0/2$ period, i.e., $\mathfrak{D}(\tau_\phi, \phi + \phi_0/2) = \mathfrak{D}(\tau_\phi, \phi)$, in agreement with weak localization theory. In contrast, when $\ell_e < |C_h|$, $L(\tau_\phi < 2\ell_e)$, the system exhibits a *positive magnetoresistance* associated with $\mathfrak{D}(\tau_\phi, \phi + \phi_0) = \mathfrak{D}(\tau_\phi, \phi)$. For the case $\ell_e < |C_h|$, $L(\tau_\phi > 2\ell_e)$, negative magnetoresistance and Aharonov–Bohm oscillations with period ϕ_0 are obtained. Note

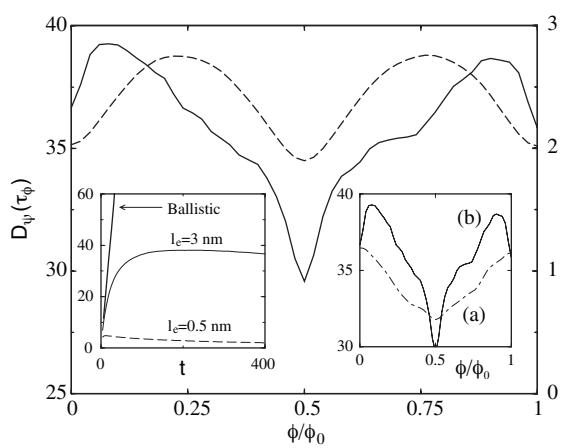

Figure 5.11 Diffusion coefficient $\mathfrak{D}(\tau_\phi, \phi/\phi_0)$ (in units of Å^2-$\gamma_0/\hbar$) for the (9, 0) nanotube evaluated at time $\tau_\phi \gg \tau_e$, for two disorder strengths, W/γ_0 = 3 and 1, such that the mean free path ($\ell_e \sim 0.5$ and 3 nm, respectively) is either shorter (dashed line) or larger (solid line) than the nanotube circumference ($|\vec{C}_h| \sim 2.3$ nm). The right y-axis is for the dashed line and the left y-axis is for the solid line. Inset: $\mathfrak{D}(\tau_\phi, \phi/\phi_0)$ for ℓ_e = 3 nm and $L(\tau_\phi) < 2\ell_e$.

that with the analytical formula for the mean free path and estimates of disorder values, we get $\ell_e \simeq 10^4 \times |C_h|$ ($|C_h|$ is the circumference of the outer nanotube in the experiment of Bachtold et al.[12]). The apparent inconsistency between the value of the mean free path and the observation of the $\phi_0/2$ Aharonov–Bohm oscillations demonstrates that the interpretation of the experiments might be delicate since the precise position of the Fermi level and contribution of inner shells remain unclear[36,37]

In fact, in the case of multiwalled carbon nanotubes, the situation is complicated. First, each shell has a different diameter, with approximately a difference of 3 Å between neighboring shells.[39,40] This might bring intricate contributions of Aharonov–Bohm phases with no clear overall oscillation period. In addition, in most cases, neighboring shells are incommensurate, one respect to another. This produces an underlying aperiodic potential for π-electron scattering, which can give rise to unusual energy-dependent magnetotransport fingerprints.[33]

5.2.3.3 *Persistent currents*

The theoretical prediction and further experimental observation of persistent currents (I_{pc}) in isolated mesoscopic rings has been one of the cornerstones of mesoscopic physics.[41,42] Such nondissipative currents result from inductive phenomena when a magnetic field is applied perpendicular to the ring. The Aharonov–Bohm effect modulates the boundary conditions of the quantum phase in a similar fashion as described in Section 5.2.1. Persistent currents can be observed if the electrons preserve their quantum coherent phase at least over the length of the ring.

Recently, Martel et al.[43] have synthetized carbon nanotube-based rings by combining chemical and ultrasonic treatments. The obtained rings formed by small bundles of single-walled nanotubes were further contacted to metallic electrodes, and a magnetotransport study was performed.[44] The authors conclude that electronic transport could be described with the conventional localization theory, and data were consistent with a phase coherence length smaller than the ring length, with no sign of periodic Aharonov–Bohm oscillations.[44] A very important issue is to investigate to which extent intrinsic properties of I_{pc} can be related to the intrinsic conduction mechanisms (ballistic vs. diffusive or localized), which can depend on the structural quality of individual tubes as well as intertube interactions in bundles.

Let us start with the basics of persistent current theory. Within the Fermi liquid framework, $I_{pc} = -\frac{1}{\phi_0}\Sigma_n \partial\varepsilon_n / \phi$ where ϕ is the flux through the ring in units of ϕ_0 and the sum has to be done over all occupied states. In the case of ballistic rings (e.g., semiconducting heterostuctures), the predicted average value of persistent current has been confirmed experimentally, in contrast with metallic rings with low mean free paths, for which a quantitative disagreement between theory and experiments remains controversial (typically $I_{pc}^{theor.} \sim 10^{-2} I_{pc}^{expts.}$). $I_{pc}(\phi)$ being an odd and periodic function of ϕ, it can

be expanded in Fourier series as[45] $I_{pc}(\phi) = \Sigma_{n=0}^{\infty} I_n.\sin(2\pi n\phi)$, where I_n is the n-th harmonic, which is given by $\frac{2I_0}{n\pi}\cos(nk_F L_{ring})$, where ($I_0 \sim e\upsilon_F/L_{ring}$, L_{ring} is the ring length). To represent the average value of persistent current, it is useful to compute $J_{quad} = \sqrt{\int_{-1/2}^{+1/2} I_{pc}^2\left(\phi\right)d\phi}$, or $J_{\phi=1/4} = \left|I_{pc}\left(\frac{1}{4}\right)\right|$, which is dominated by the first harmonic.

In conventional mesoscopic systems, the mean free path ℓ_e can be used to distinguish between the ballistic and diffusive regimes, thereby enabling one to understand the evolution of persistent currents with disorder as far as their amplitude and oscillation period are concerned. Different regimes can be defined whether $\ell_e \gg L_{ring}$ (ballistic regime), $\ell_e < L_{ring}$ (diffusive regime), or $\xi \simeq N_c\ell_e < L_{ring}$ (localized regime where ξ is the localization length).[45] The first regime is associtaed with an average persistent current given by $\sim e\upsilon_F/L_{ring}$. In Figure 5.13, such a case is shown for (6, 6)-based tori of different lengths (Figure 5.12).[46] The persistent current maximum intensity for a defect-free (6, 6) tube with 82 unit cells ($L_{ring} \simeq 20$ nm) is then found to be $I_0 = 2e\upsilon_F/L_{ring} \simeq 15$ μA.

In the case of a diffusive regime, the average persistent current on a single eigenstate J_n^{typ} (average performed on torus length, disorder configurations, and magnetic flux) is expected to be given by the law $\sqrt{<\overline{J_n^2\left(\phi\right)}>W, L_{ring}} \sim \sqrt{\Delta E_c}\ /\ \phi_0$ (where $\Delta = h\upsilon_F/L_{ring}$ is the average distance between eigenstates), whereas the total typical current writes $J_{typ} = \Sigma_n J_{typ}^n \sim \frac{E_c}{\phi_0} = \frac{e\upsilon_F\ e}{L_{ring}^2}$ (where $E_c = \hbar\upsilon_F\ell_e/L_{ring}^2$ is the Thouless energy).[45,47,48] However, for weak enough disorder such that $\ell_e \leq L_{ring}$, the average behavior of persistent currents is much more difficult to anticipate analytically. Whenever $\ell_e < L_{ring}$,[49] one could expect that the law $\sim e\upsilon_F\ell_e/L_{ring}^2$ should still be satisfied to some extent so that the amplitude should remain reduced roughly by a $\sim \ell_e/L_{ring}$ factor with respect to the ballistic case.

Assuming an Anderson-type disorder, such a law will suppose some $(\gamma_0/W)^2$ dependence in the quasi-ballistic regime. In Figure 5.14, the typical persistent current is plotted as a function of ℓ_e for a (6, 6) tube (radius $\simeq 258$ nm) with length in the order of $L_{ring} \simeq 18.4$ nm ($\Delta \sim 0.205$ eV). Results obtained for $J_{1/4}$ and J_{quad} clearly demonstrate that the $1/W^2$ law is not satisfied while $2\ell_e > L_{ring}$. Actually, a simple criterion can be found to describe the damping of persistent currents in the quasi-ballistic regime. For a given disorder strength (and corresponding ℓ_e), harmonics of rank n, such that $\ell_e > nL_{ring}$, will remain insensitive to disorder (as in the ballistic case), whereas others will be exponentially damped. A qualitative trend of persistent current evolutions with disorder can thus be extracted thanks to the knowledge of the dependence of ℓ_e with disorder. As shown in Section 5.2.3, strong

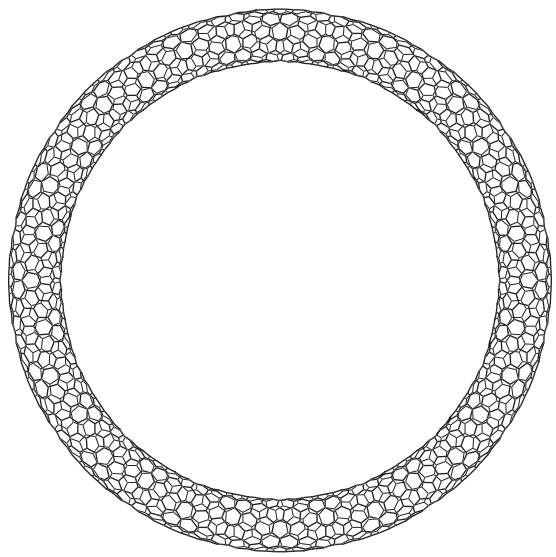

Figure 5.12 Carbon nanotube-based torus, closed by covalent bonding.

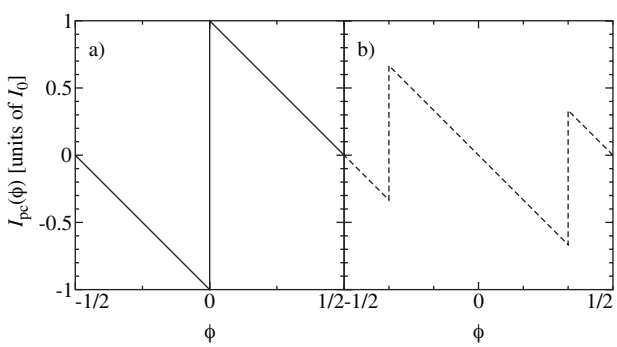

Figure 5.13 Magnetic flux dependence of persistent currents for two (6, 6) nanotube-based torii (Figure 5.12) of different lengths.[46]

fluctuations of ℓ_e occur for small Fermi level shifts, so that *giant fluctuations of persistent currents are predicted theoretically.*

We now discuss the case of more complex geometry, in which boundary conditions of the rings are driven by noncovalent bonding (Figure 5.15, left). This case is important since synthetized nanotube-based rings are not closed by covalent bonds. The Hamiltonian of the ring is now written

$$H = -\gamma_0 \sum_{p_i, P_{j(i)}} |p_i\rangle\langle p_j| \exp\left(i\varphi_{ij}\right) - \gamma_1 \sum_{<p_i, p_k>} \left(|p_i\rangle\langle p_k| + |p_k\rangle\langle p_i|\right) \exp\left(i\varphi_{ik}\right) \tag{5.19}$$

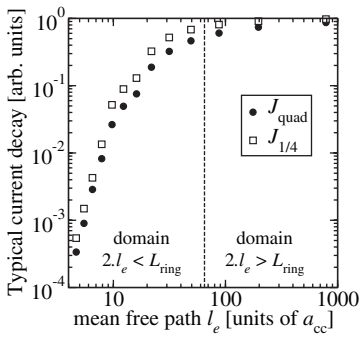

Figure 5.14 Evolution of the typical persistent current intensity with ℓ_e computed with the analytical form defined in Section 5.2.3.

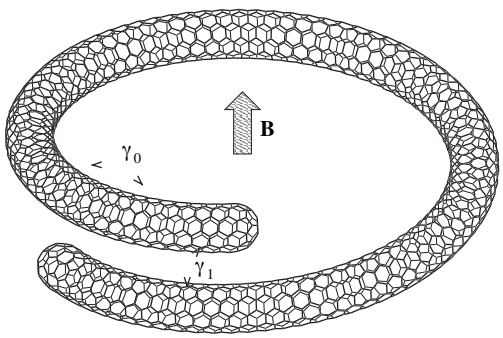

Figure 5.15 Carbon nanotube-based coil that exihibits some weak noncovalent self-interaction at the boundaries.

where $\varphi_{ij} = 2\pi\left(\frac{z_j - z_i}{L_{\text{ring}}}\right)\phi$, and $|p_i\rangle$ and $|p_j\rangle$ define the π-orbitals localized at sites z_i and z_j ($\phi = \phi/\phi_0$), $\gamma_1 = V_{\text{int}} \exp\left(\frac{d-\delta}{l}\right)$, and d denotes the relative distance between the two orbitals. Remaining parameters are $V_{\text{int}} = 0.36$ eV, $\delta = 3.34$ Å, and $l = 0.45$ Å (site energies are given in units of γ_0).

Results show that in most cases, intertube interaction has little effect on persistent currents if two torii are considered, and if they are not commensurate. Commensurability between torii (i.e., translation invariance of tube–tube interation, with a unit cell much smaller than torus length) might, however, significantly affect persistent currents because of degeneracy splitting induced by intertube coupling (see Latil et al.[46]). For noncovalent torii, as described in Figure 5.15, a pronounced damping of current amplitude is found (Figure 5.16), and the damping will be dependent on L_{stick}, the length of the self-interacting region of the coil, whereas d_{stick} gives the spacing

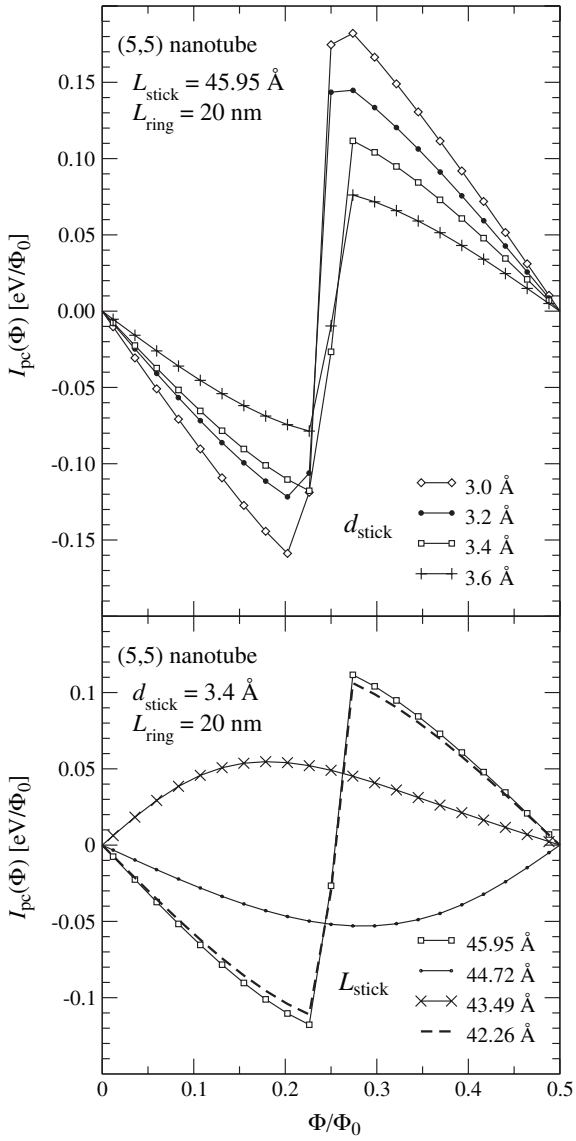

Figure 5.16 Flux-dependent persistent currents as a function of stick length (L_{stick}) along with the interaction between nearest neighboring orbitals come from noncovalent bonding, whereas d_{stick} denotes their relative interspacing.

distance between frontier orbitals. Typical intensity is reduced by roughly one to two orders of magnitudes, compared to the case of covalent bonding (Figure 5.12).

5.3 Experimental results

As discussed in the previous sections, carbon nanotubes, either metallic or semiconducting, are predicted to possess novel magnetic properties. The remaining sections of this chapter review experimental studies of carbon nanotubes performed to date, which have confirmed or challenged some of the predictions, including magnetic (Section 5.3.1), magneto-optical (Section 5.3.2), and magnetotransport (Section 5.3.3) properties.

5.3.1 Magnetization

One of the earliest experimental studies on magnetic properties of carbon nanotubes was performed by Wang et al.[50,51] Through magnetic susceptibility measurements on a bulk sample of buckybundles, they concluded that these bundles are diamagnetic and $|\chi_{\parallel}/\chi_{\perp}| \approx 1.1$. (This anisotropy is opposite of the prediction that $|\chi_{\parallel}| < |\chi_{\perp}|$.) Heremans and coworkers[52,53] reported results of a systematic study on the magnetic susceptibilities of diamond, graphite, C_{60}, and multiwalled carbon nanotubes as functions of temperature and magnetic field. It was found that the χ of nanotubes was about half of that of graphite, which is known to be very large ($\approx -3 \times 10^5$ emu/g for $H \parallel$ c-axis below 100 K) due to the existence of the aromatic-like π-electrons that are absent in diamond; it showed similar temperature and field dependences to graphite (Figure 5.17). Ramirez et al.[54] reported that the χ of carbon nanotube bundles is even larger than that of graphite on a per carbon basis. Results of these early studies are basically consistent with the notion that carbon nanotubes are rolled-up cylinders of graphene sheets that should show large diamagnenetism associated with the ring currents flowing along the hexagonal rings of carbon,[55] but the samples studies were randomly oriented bundles and only average magnetic properties were probed.

Chauvet et al. studied magnetic properties of *aligned* multiwalled carbon nanotubes in films at various temperatures and magnetic field orientations.[57] They found that the nanotubes were diamagnetic and anisotropic. However, the results indicated that $|\chi_{\parallel}| < |\chi_{\perp}|$ at all temperatures (similar to the work on buckybundles[51]). It was claimed[55,57] that the large diamagnetic suseptibility parallel to the tube axis may be due to the additional ring current along the circumference, but this behavior was clearly in contradiction with the predictions by Ajiki and Ando[25,27] and Lu,[4] described in detail in the previous section. More recent experimental studies on aligned multiwalled carbon nanotubes[56,58,59] unanimously showed behavior in agreement with $|\chi_{\parallel}| > |\chi_{\perp}|$ (see, e.g., Figure 5.18). Kotosonov[56] argues that the confusion might have been because of inaccurate estimation of nanotube orientations in the samples used in earlier studies.

An interesting consequence of anisotropic magnetic susceptibilities is *magnetic alignment*. It has been demonstrated that paramagnetic[60] and diamagnetic[61] molecules with anisotropic susceptibilities as well as proteins can be effectively aligned by external magnetic fields if the magnetic energy

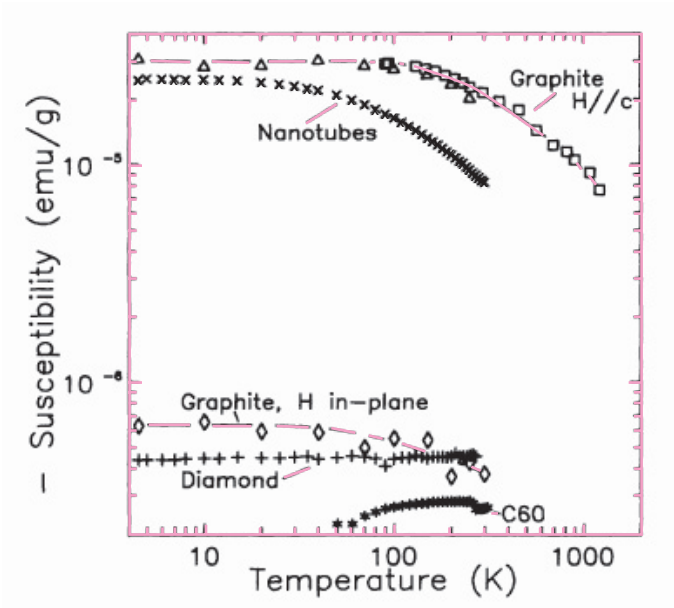

Figure 5.17 Temperature dependence of the magnetic susceptibility of various carbon materials, including bundles of multiwalled carbon nanotubes. (Adopted from J. Heremans et al., *Phys. Rev. B*, 49, 15122, 1994.)

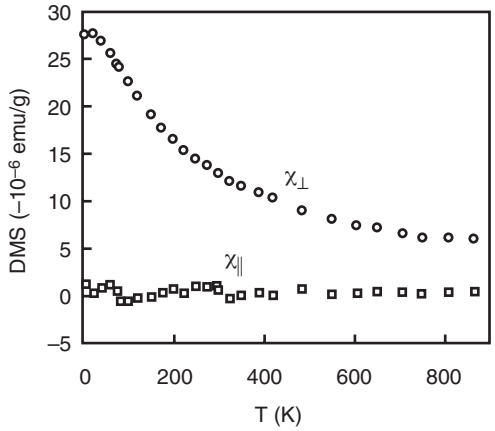

Figure 5.18 The parallel and perpendicular magnetic susceptibilities of aligned multiwalled carbon nanotubes. (Adopted from A. S. Kotosonov, *JETP Lett.*, 70, 476, 1999.)

dominates the thermal energy. A. Fujiwara and cowokers were the first to succeed in fabricating magnetically aligned multiwalled nanotube films by drying nanotubes dispersed in methanol in a 7-T field.[58] Kimura et al. used a similar technique (in a 10-T field) to obtain electrically and mechanically

anisotropic multiwalled carbon nanotube/polymer composites.[62] Furthermore, M. Fujiwara et al.[63,64] succeeded in magnetically aligning *individual* multiwalled carbon nanotubes and estimated the degree of diamagnetic anisotropy to be $\chi_{\parallel} - \chi_{\perp} \sim (9 \pm 5) \times 10^{-6}$ emu/mol ($\chi_{\parallel} < \chi_{\perp} < 0$).

More recently, single-walled carbon nanotubes have been magnetically aligned.[65–67] Walters et al. produced thin membranes comprised of highly aligned single-walled nanotubes by producing a SWNT suspension, placing the suspension in magnetic fields as high as 25 T and filtering the suspension in the magnetic field.[65,66] Zaric et al. demonstrated magnetic alignment of SWNTs of specific chiralities using micelle-suspended SWNTs in aqueous solutions.[11,67] Through analysis of the photoluminescence and absorption spectra in magnetic fields, in conjunction with atomic force microscopy (AFM) measurements to determine the length distribution of the nanotubes, they were able to estimate the diamagnetic anisotropy $\chi_{\parallel} - \chi_{\perp}$ to be $\sim 1.4 \times 10^{-5}$ emu/mol for 1-nm-diameter semiconducting nanotubes. This value is similar to the predicted values, i.e., 1.9×10^{-5} emu/mol[25] and 1.5×10^{-5} emu/mol.[4]. Furthermore, the extracted degree of alignment showed that tubes of larger diameters d align better, which is in qualitative agreement with the prediction, i.e., $|\chi_{\parallel} - \chi_{\perp}| \propto d$.[4,25] See Section 5.2 for more data and analyses by Zaric et al.

5.3.2 Magneto-optics

As described in Section 5.2.1, when a SWNT is threaded by a magnetic flux ϕ, its band structure is predicted to depend on ϕ/ϕ_0: the band gap oscillates with period ϕ_0, and ϕ/ϕ_0-dependent splitting. Consequences of these effects are expected to appear in various quantities, but most prominently in interband optical spectra as peak shifts and splittings.[2,7,8] The Aharonov–Bohm-induced VHS splittings are due to degeneracy lifting between the K and K' points, and for semiconducting nanotubes, the amount of splitting is given by $\Delta_{KK'} = 6\Delta_g\phi/\phi_0$ (where Δ_g is the zero-field band gap) when $\phi/\phi_0 < 1/6$. For a typical semiconducting SWNT with 1 nm diameter, this yields $\Delta_{KK'} \sim 1$ meV/T.

Recent success in preparing individually suspended SWNTs in aqueous solutions led to the observation of chirality-dependent peaks in absorption and photoluminescence (PL) spectra[68] and to complete chirality assignments.[69] This has opened ways to perform spectroscopy of SWNTs of specific chiralities. Zaric et al.[11,67] recently utilized such samples in a series of high-field magneto-optical studies, directly verifying some of the predicted band structure modifications due to the Aharonov–Bohm effect. We summarize some of the highlights of their work in this section.

Zaric and coworkers measured absorption and PL in micelle-suspended SWNTs at magnetic fields (B) up to 45 T. The observed peaks exhibited significant changes with increasing B. In absorption they observed splittings in some of the first subband transition peaks. The amount of splittings (30 to 40 meV at 45 T) was consistent with the expected splitting. Splittings were

not resolvable in the second subband transitions due to their larger line widths (~100 meV). Magneto-PL showed red shifts with increasing B for all observed peaks, the amount of which was diameter dependent in a predicted way. Detailed PL simulations, taking into account B-induced alignment of nanotubes, thermal population, and Aharonov–Bohm-induced splittings, successfully reproduced the observed spectra, supporting their interpretation. However, it is important to point out that 45 T is not high enough to reveal a full period of the Aharonov–Bohm effect. For a typical nanotube diameter of 1 nm, 45 T corresponds to $\phi/\phi_0 \sim 10^{-2}$.

Figure 5.19a shows polarization ($\vec{P}$)-dependent magnetoabsorption for the first subband (E_1H_1) transitions. The solid and dashed lines are for parallel ($\vec{B} \parallel \vec{P}$) and perpendicular ($\vec{B} \perp \vec{P}$) polarizations, respectively. The field induces drastic changes in the spectrum. First, note that no traces are intentionally offset, so the P-dependent vertical shifts are real; i.e., the B increases (decreases) the absorption in the parallel (perpendicular) case, resulting in large optical anisotropy. At 45 T, the absorption coefficient ratio ($\alpha_\parallel/\alpha_\perp$) is ~4. The optical anisotropy, defined as $\alpha_\parallel - \alpha_\perp/\alpha_\parallel + \alpha_\perp$, is plotted vs. energy for 0, 20, and 45 T in Figure 5.19b, where the dotted lines are raw data and the solid lines are polynomial fits. At a given B, the anisotropy is larger for lower energies (corresponding to larger diameters). Since perpendicularly polarized light is not absorbed,[2] this indicates that larger-diameter tubes align better. The field also induces spectral modifications. Each absorption peak is seen to become broader with increasing B, and finally, some of the peaks split in the highest field range, i.e., 30 to 45 T, only in the $\vec{B} \parallel \vec{P}$ case (Figure 5.19c).

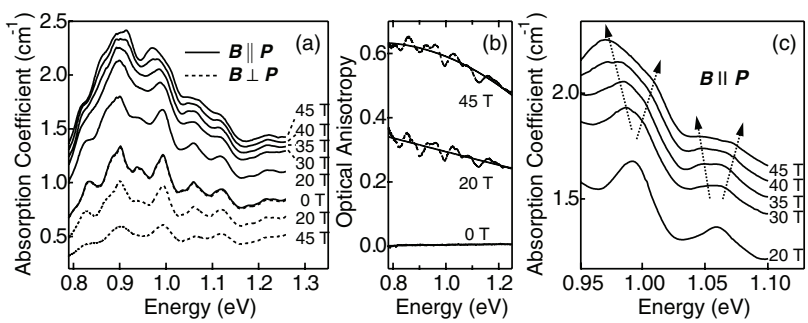

Figure 5.19 (a) Polarization-dependent magnetoabsorption spectra for micelle-suspended SWNTs in D_2O in the spectral range of the first subband (E_1H_1) transitions. Solid and dashed lines are for parallel ($\vec{B} \parallel \vec{P}$) and perpendicular ($\vec{B} \perp \vec{P}$) polarizations, respectively. No traces are offset. (b) Optical anisotropy, defined as $\alpha_\parallel - \alpha_\perp/\alpha_\parallel + \alpha_\perp$, vs. photon energy. For a given field, the larger the nanotube diameter, the larger the optical anisotropy. (c) An expanded plot of data for the $\vec{B} \parallel \vec{P}$ case from 20 to 45 T, showing field-induced splitting of two absorption peaks.

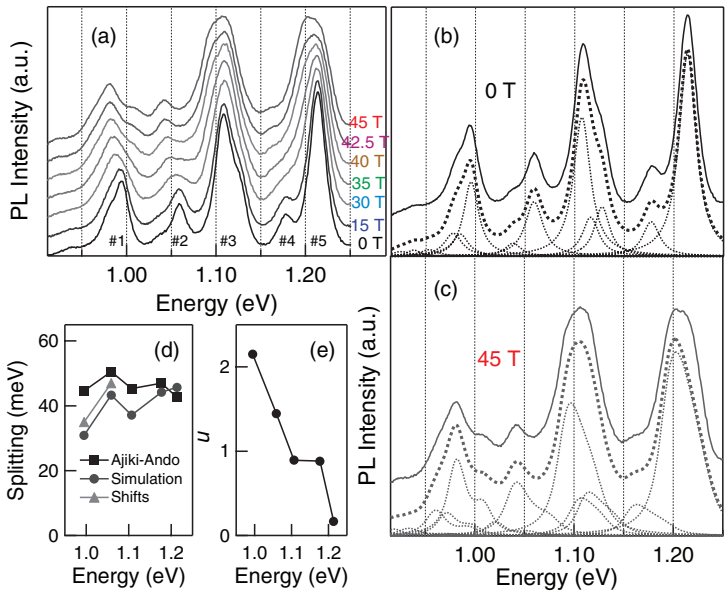

Figure 5.20 (a) Magneto-PL spectra for micelle-suspended SWNTs in D_2O, excited with a 633-nm beam. The traces are shifted vertically for clarity. The chiralities of the most visible peaks are #1, (10, 3); #2, (8, 6); #3, (7, 6); #4, (10, 2); and #5, (7, 5). As the field increases, all peaks red shift. (b, c) Measured (solid line) and theoretical (thick dotted line) PL spectra at (b) 0 T and (c) 45 T. Individual theoretical PL peaks are also plotted as thin dotted lines. (d) Ajiki–Ando splittings obtained from predictions (solid line), simulations (solid circles), and peak shifts (solid triangles). (e) The values of the alignment parameter u (see the text for definition) at 45 T for the five main PL peaks, obtained from data analyses and simulations. Significant spectral changes are expected only when $u > 0.707$ (see text).

Figure 5.20a shows magneto-PL spectra up to 45 T, excited by a 633-nm He-Ne laser. The chiralities n, m of the main five peaks, numbers 1 to 5, are indicated in the caption. It can be seen that all PL peaks exhibit interesting spectral evolution with B. Specifically, all peaks shift to lower energy, and the shift is more obvious for lower-energy peaks (i.e., numbers 1 and 2) or larger-diameter tubes. The 0 and 45 T data are replotted as solid lines in Figure 5.20b and c, respectively, together with the simulated total (thick dotted lines) and individual (thin dotted lines) PL peaks. Magnetic field-induced red shifts, peak broadenings, and splittings are clearly visible.

These observations can be explained in terms of the Aharonov–Bohm effect only if we take into account the magnetic alignment of nanotubes. Unlike Zeeman splitting, the amount of Aharonov–Bohm-induced splitting depends on the angle between the tube and the field and can reach the predicted value, $\Delta_{KK'} = 6\Delta_g\phi/\phi_0$, only when the tube is completely aligned with B. This explains why significant spectral changes were observed in absorption only for P parallel to B. The nanotubes align due to their highly

anisotropic magnetic susceptibilities (see Section 5.2.2). Using the Maxwell–Boltzmann statistics, the probability density that a given nanotube, consisting of N moles of carbon atoms, is at an angle between θ and $\theta + d\theta$ relative to the field is (see, e.g., Walters et al.[65]):

$$P(\theta)d\theta = \frac{\exp\left(-u^2 \sin^2\theta\right)d\theta}{\int_0^{\pi/2} \exp\left(-u^2 \sin^2\theta\right)d\theta}, \tag{5.20}$$

where $[B^2N(\chi_\parallel - \chi^\perp)/k_BT]^{1/2}$, k_B is the the Boltzmann constant, and T is the temperature. The quantity u is a dimensionless measure of alignment, containing the ratio of the alignment energy to the thermal energy and completely determines the angular distribution for a given chirality at given B and T. As B increases, u increases and, consequently, the probability that the tube is at a small θ increases. The existence of angle distribution prevents the full amount of red shift, $\Delta E_{PL}^{\text{theory}} = \Delta_{KK'}/2 = 3\Delta_g\phi/\phi_0$; instead, the observed PL shift is given by $\Delta E_{PL}^{\text{experiment}} = \Delta E_{PL}^{\text{theory}} \cos\theta^*$. Here θ^* is the angle at which $P(\theta)$ is maximum and can be expressed in terms of u:

$$\theta^* = \begin{cases} \pi/2 & \text{for} \quad u \le \dfrac{1}{\sqrt{2}} \\ \arcsin\left(1/\sqrt{2}u\right) & \text{for} \quad u > \dfrac{1}{\sqrt{2}} \end{cases}. \tag{5.21}$$

Equation 5.21 suggests that absorption and PL will not show significant shifts until u reaches the critical value ($\sqrt{2} \approx 0.707$). In addition, since u is expected to increase with the tube diameter[4,27] (Section 5.2.2), one can expect stronger alignment for larger-diameter tubes, and lower-energy peaks should start showing B dependence at lower B, consistent with the data.

In order to use the experimentally determined values of u to estimate the magnetic susceptibility anisotropy through using $u = [B^2N(\chi_\parallel - \chi_\perp)/k_BT]^{1/2}$, the length distribution of the nanotubes was measured. The nanotubes were deposited onto a SiO_2-covered wafer by simply dipping the wafer into the sample solution 5 to 10 times. The wafer was then rinsed and imaged using an atomic force microscopy. The obtained length histogram had a maximum at about 300 nm. Taking into account that, for all the five peaks, the diameter of the corresponding nanotube was ~1 nm, Zaric et al.[11,67] obtained $\chi_\parallel - \chi_\perp \sim 1.4 \times 10^{-5}$ emu/mol, similar to the predicted values, i.e., 1.9×10^{-5} emu/mol[27] and 1.5×10^{-5} emu/mol.[4]

5.3.3 Magnetotransport

As shown in the theoretical part, the application of a magnetic field is a precious tool for clarifying the role of quantum interferences in magnetotransport.[38] The first experimental magnetotransport study on carbon nanotubes was performed by Langer et al.[70] on large-diameter MWNTs, for fields applied perpendicular to the tube axis. The observation of negative magnetoresistance, together with universal conductance fluctuations, was compatible with the contribution of quantum interference effects in the diffusive regime and in the weak localization framework. A few years later, Bachtold et al.[12] provided additional evidences of such a scenario when measuring negative magnetoresistance superimposed onto $\phi_0/2$ periodic Aharonov–Bohm oscillations, by applying a field parallel to the tube axis.

In that study, the conduction regime was extrapolated to be diffusive with ℓ_e in the order of the tube circumference, while the coherence length was a few times larger and was attributed to coulomb dephasing effects in the perturbative regime. In the same paper,[12] the authors also presented superimposed oscillations of a much smaller period ($\phi_0/10$), which did not find any conclusive understanding.

Similarly, other groups[13,14,71] reported on different oscillation periods as well as changes from positive to negative magnetoresistance. The authors proposed an interpretation contradictory to Bachtold et al.[12] in the sense that the magnetoresistance modulations were ascribed to band structure effects (Section 5.2.1) and transport mechanism remained ballistic, with no quantum interference contributions.

Let us discuss with simple arguments the scenario outlined so far. The experiments performed by Bachtold et al.[12] on MWNTs with a diameter in the order of 20 nm appear to be well described by conventional weak localization theory (Figure 5.21). In this work, four-probe resistance was measured on two samples. First, sample 1 (diameter = 17 nm, or $|C_h| \simeq 53$ nm, and interelectrode spacing = 170 nm) was found to display negative magnetoresistance together with $\phi_0/2$ periodic oscillations. The zero-flux resistance was given by $R_{4c} \simeq 30k\Omega$. As usual in the theory of diffusive systems, the resistance can be written as $R_{4c}\ h/N_\perp 2e^2)\ (1 - T)/T$. By further assuming that $N_\perp = 2$ and given $h/2e^2 = 13k\Omega$, the transmission coefficient is found to be $T \sim 0.174$, so that the mean free path $\ell_e \sim 35$ nm $\leq |C_h|$. This short derivation consistently shows that the obtained value for mean free path agrees with weak localization requirements. Following the same argument for sample 2 (diameter = 13 nm, or $|C_h| \simeq 40$ nm, and interelectrode spacing = 170 nm), and given that $R_{4c} \simeq 2.4k\Omega$ at zero flux, we can deduce (by still assuming $N_\perp = 2$) a transmission coefficient $T \simeq 0.728$. In this case, $\ell_e \sim 450$ nm, or $\ell_e \sim 10|C_h|$. It thus appears that the extrapolated transport length scale does not allow us to strictly apply conventional weak localization theory. Amazingly, sample 2 shows a much smaller oscillation period, $\phi_0/10$, seemingly superimposed onto the $\phi_0/2$ oscillations, whose convincing interpretation is still lacking.

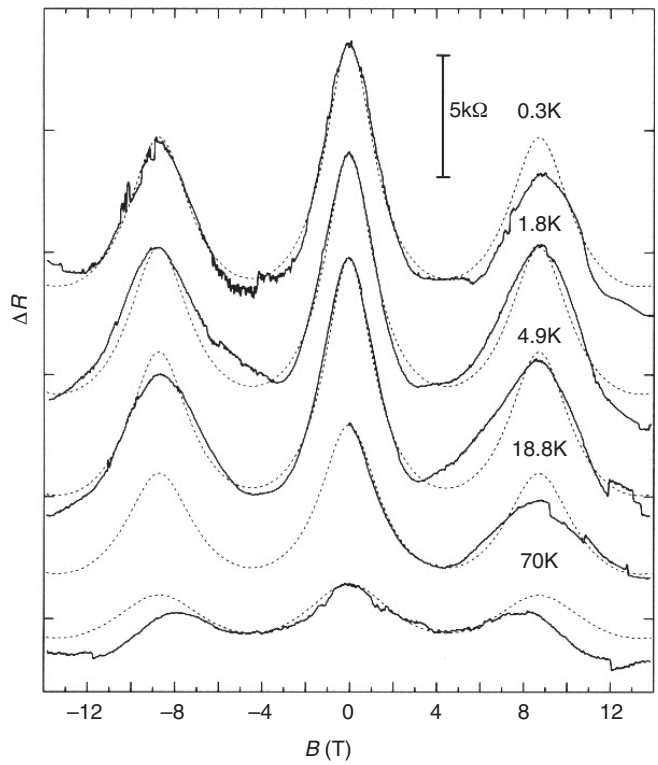

Figure 5.21 Magnetoresistance of a MWNT measured in the parallel configuration. (From Bachtold, A. et al., *Nature*, 397, 673, 1999.)

By the same argument, one can verify that other seemingly contradictory experiments (or interpretations)[13] are indeed achieved in a regime out of the strict applicability conditions of weak localization theory. In addition, it has to be noticed that if $\phi_0/2$ oscillations are observed in a magnetotransport experiment, one cannot disregard the modifications of the band structure, as detailed in Section 5.2.1, and thus the whole theory should simultaneously account for both magnetic effects on electronic structure and quantum interference effects on transport, as discussed in Roche and Saito.[72]

Very recently, three groups have further performed novel magnetotransport experiments on carbon nanotubes. Ferorov et al. have measured magnetotransport on *double-walled* nanotubes with 3 nm diameter while varying the magnetic field orientation and applied gate voltage.[73] With an estimated modulation of the position of the Fermi level by about 50 meV, the magnetotransport fingerprints were shown to switch from a regime fully dominated by weak localization (negative magnetoresistance) to a more complex regime where both weak localization and band structure effects contribute. Coskun et al. have studied magnetotransport in the coulomb blockade regime, where evidence for ϕ_0 periodic oscillations of the energy gap was given for

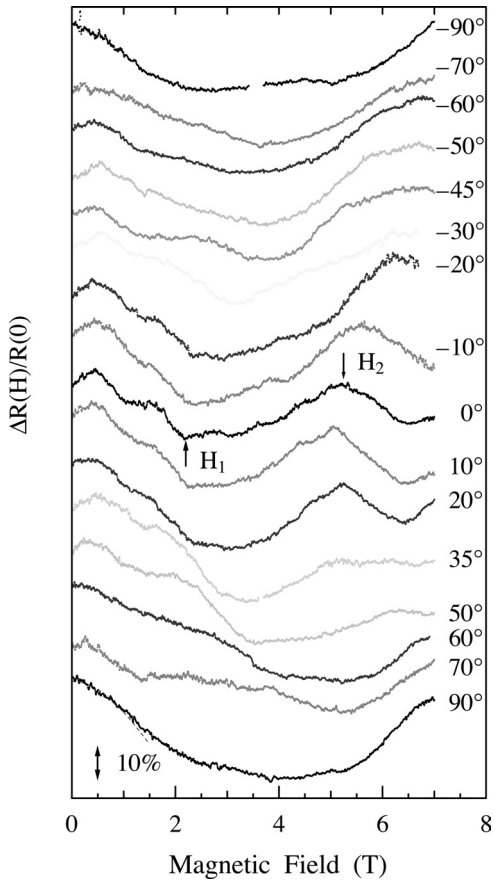

AU: Please cite figure in text.

Figure 5.22 Magnetoresistance of a MWNT as a function of magnetic field orientation with respect to tube axis. (From A. Fujiwara et al., *Phys. Rev. B*, 60, 13492, 1999.)

large-diameter multiwalled nanotubes weakly coupled to Au/Cr metallic contacts.[18] Furthermore, most recently, by achieving a good ohmic contact between single-walled metallic nanotube and Pt electrodes, Cao et al. have observed *B*-dependent modulations of the Fabry–Perot interference patterns in single-walled carbon nanotubes in the ballistic transport regime.[19]

All these experimental studies confirm the subtle interplay between quantum interference phenomena and magnetic field-dependent band structure in carbon nanotubes. However, despite these results, several unanswered questions remain, such as the relation between magnetotransport oscillations and elastic and inelastic scattering in carbon nanotubes, the contribution of intershell coupling, and the superposition of various Aharonov–Bohm phases of different origins. The physics of excitons in carbon nanotubes subjected to external magnetic fields also appears as an interesting problem to consider.

Acknowledgments

J.K. thanks the National Science Foundation (grants DMR-0134058 and DMR-0325474) and the Robert A. Welch Foundation (grant C-1509) for support. S.R. acknowledges F. Triozon and S. Latil for valuable discussions and the research grant from the French Ministry of Research under ACI project *TransNanoFils*.

References

1. H. Ajiki and T. Ando, Electronic states of carbon nanotubes, *J. Phys. Soc. Jpn.* 62, 1255 (1993).
2. H. Ajiki and T. Ando, Aharonov-Bohm effect in carbon nanotubes, *Physica B* 201, 349 (1994).
3. W. Tian and S. Datta, Aharonov-Bohm-type effect in graphene tubules: a Landauer approach, *Phys. Rev. B* 49, 5097 (1994).
4. J. P. Lu, Novel magnetic properties of carbon nanotubes, *Phys. Rev. Lett.* 74, 1123 (1995).
5. H. Ajiki and T. Ando, Energy bands of carbon nanotubes in magnetic fields, *J. Phys. Soc. Jpn.* 65, 505 (1996).
6. J. Jiang, J. Dong, and D. Y. Xing, Zeeman effect on the electronic spectral properties of carbon nanotubes in an axial magnetic field, *Phys. Rev. B* 62, 13209 (2000).
7. S. Roche, G. Dresselhaus, M. S. Dresselhaus, and R. Saito, Aharonov-Bohm spectral features and coherence lengths in carbon nanotubes, *Phys. Rev. B* 62, 16092 (2000).
8. F. L. Shyu, C. P. Chang, R. B. Chen, C. W. Chiu, and M. F. Lin, Magnetoelectronic and optical properties of carbon nanotubes, *Phys. Rev. B* 67, 045405 (2003).
9. T. Ando, Excitons in carbon nanotubes revisited: dependence on diameter, Aharonov-Bohm flux, and strain, *J. Phys. Soc. Jpn.* 73, 3351 (2004).
10. Y. Aharonov and D. Bohm, Significance of electromagnetic potentials in the quantum theory, *Phys. Rev.* 115, 485 (1959).
11. S. Zaric, G. N. Ostojic, J. Kono, J. Shaver, V. C. Moore, M. S. Strano, R. H. Hauge, R. E. Smalley, and X. Wei, Optical signatures of the Aharonov-Bohm phase in single-walled carbon nanotubes, *Science* 304, 1129 (2004).
12. A. Bachtold, C. Strunk, J.-P. Salvetat, J.-M. Bonard, L. Forró, T. Nussbaumer, and C. Schönenberger, Aharonov-Bohm oscillations in carbon nanotubes, *Nature* 397, 673 (1999).
13. A. Fujiwara, K. Tomiyama, H. Suematsu, M. Yumura, and K. Uchida, Quantum interference of Electrons in multiwall carbon nanotubes, *Phys. Rev. B* 60, 13492 (1999).
14. J.-O. Lee, J.-R. Kim, J.-J. Kim, J. Kim, N. Kim, J. W. Park, and K.-H. Yoo, Observation of magnetic-field-modulated energy gap in carbon nanotubes, *Solid State Commun.* 115, 467 (2000).
15. A. Kanda, S. Uryu, K. Tsukagoshi, Y. Ootuka, and Y. Aoyagi, Magnetic field dependence of coulomb oscillations in metal/multi-wall carbon nanotube/metal structures, *Physica B* 323, 246 (2002).

16. E. D. Minot, Y. Yaish, V. Sazonova, and P. L. McEuen, Determination of electron orbital magnetic moments in carbon nanotubes, *Nature* 428, 536 (2004).
17. P. Jarillo-Herrero, S. Sapmaz, C. Dekker, L. P. Kouwenhoven, and H. S. J. van der Zant, Electron-hole symmetry in a semiconducting carbon nanotube quantum dot, *Nature* 429, 389 (2004).
18. U. C. Coskun, T.-C. Wei, S. Vishveshwara, P. M. Goldbart, and A. Bezryadin, h/e magnetic flux modulation of the energy gap in nanotube quantum dots, *Science* 304, 1132 (2004).
19. J. Cao, Q. Wang, M. Rolandi, and H. Dai, Aharonov-Bohm interference and beating in single-walled carbon-nanotube interferometers, *Phys. Rev. Lett.* 93, 216803 (2004).
20. R. Saito, G. Dresselhaus, and M. S. Dresselhaus, *Physical Properties of Carbon Nanotubes*, Imperial College Press, London (1998).
21. S. Roche, Quantum transport by means of O(N) real-space methods, *Phys. Rev. B* 59, 2284 (1999).
22. T. Seri and T. Ando, Boltzmann conductivity of a carbon nanotube in magnetic fields, *J. Phys. Soc. Jpn.* 66, 169 (1997).
23. T. Ando and T. Seri, Quantum transport in a carbon nanotube in magnetic fields, *J. Phys. Soc. Jpn.* 66, 3558 (1997).
24. L. Wang, P. S. Davids, A. Saxena, and A. R. Bishop, Quasiparticle energy spectra and magnetic response of certain curved graphitic geometries, *Phys. Rev. B* 46, 7175 (1992).
25. H. Ajiki and T. Ando, Magnetic properties of carbon nanotubes, *J. Phys. Soc. Jpn.* 62, 2470 (1993).
26. P. S. Davids, L. Wang, A. Saxena, and A.R. Bishop, Magnetic ordering transition of electrons on mesoscopic tubes, *Phys. Rev. B* 48, 17545 (1993).
27. H. Ajiki and T. Ando, Magnetic properties of ensembles of carbon nanotubes, *J. Phys. Soc. Jpn.* 64, 4382 (1995).
28. C. T. White and T. N. Todorov, Carbon nanotubes as long ballistic conductors, *Nature* 393, 240 (1998).
29. T. Ando and T. Nakanishi, Impurity scattering in carbon nanotubes: absence of back scattering, *J. Phys. Soc. Jpn.* 67, 1704 (1998).
30. T. Ando, T. Nakanishi, and R. Saito, Berry's phase and absence of back scattering in carbon nanotubes, *J. Phys. Soc. Jpn.* 67, 2857 (1998).
31. S. Latil, S. Roche, D. Mayou, and J.-C. Charlier, Mesoscopic transport in chemically doped carbon nanotubes, *Phys. Rev. Lett.* 92, 256805 (2004).
32. J. W. Mintmire and C. T. White, Universal density of states for carbon nanotubes, *Phys. Rev. Lett.* 81, 2506 (1998).
33. F. Triozon, S. Roche, A. Rubio, and D. Mayou, Electrical transport in carbon nanotubes: role of disorder and helical symmetries, *Phys. Rev. B* 69, 121410(R) (2004).
34. K. Liu, P. Avouris, R. Martel, and W. K. Hsu, Electrical transport in doped multiwalled carbon nanotubes, *Phys. Rev. B* 63, 161404(R) (2001).
35. V. Krsti, S. Blumentritt, J. Muster, S. Roth, and A. Rubio, Role of disorder on transport in boron-doped multiwalled carbon nanotubes, *Phys. Rev. B* 67, 041401(R) (2003).
36. S. Roche, F. Triozon, A. Rubio, and D. Mayou, Conduction mechanisms and magnetotransport in multiwalled carbon nanotubes, *Phys. Rev. B* 64, 121401(R) (2001).

37. S. Roche, F. Triozon, A. Rubio, and D. Mayou, Electronic conduction in multi-walled carbon nanotubes: role of intershell coupling and incommensurability, *Phys. Lett. A* 285, 94 (2001).
38. A. G. Aronov and Y. V. Sharvin, Magnetic flux effects in disordered conductors, *Rev. Mod. Phys*. 59, 755 (1987).
39. R. Saito, G. Dresselhaus, and M. S. Dresselhaus, Electronic structure of double-layer graphene tubules, *J. Appl. Phys.* 73, 494 (1993).
40. J. Charlier and J. Michenaud, Energetics of multilayered carbon tubules, *Phys. Rev. Lett.* 70, 1858 (1993).
41. M. Büttiker, Y. Imry, and R. Landauer, Josephson behavior in small normal one-dimensional rings, *Phys. Lett. A* 96, 365 (1983).
42. L. P. Lévy, G. Dolan, J. Dunsmuir, and H. Bouchiat, Magnetization of mesoscopic copper rings: evidence for persistent currents, *Phys. Rev. Lett.* 64, 2074 (1990).
43. R. Martel, H. R. Shea, and P. Avouris, Rings of single-walled carbon nanotubes, *Nature (London)* 398, 299 (1999).
44. H. R. Shea, R. Martel, and P. Avouris, Electrical transport in rings of single-wall nanotubes: one-dimensional localization, *Phys. Rev. Lett.* 84, 4441 (2000).
45. Y. Imry, *Introduction to Mesoscopic Physics*, Oxford University Press, New York (1997).
46. S. Latil, S. Roche, and A. Rubio, Persistent currents in carbon nanotube based rings, *Phys. Rev. B* 67, 165420 (2003).
47. H. Bouchiat and G. Montambaux, *J. Phys. (Paris)* 50, 2695 (1989).
48. G. Montambaux, H. Bouchiat, D. Sigeti, and R. Friesner, Persistent currents in mesoscopic metallic rings: ensemble average, *Phys. Rev. B* 42, 7647 (1990).
49. A. Altland, Y. Gefen, and G. Montambaux, What is the Thouless energy for ballistic systems?, *Phys. Rev. Lett.* 76, 11301133 (1996).
50. X. K. Wang, X. W. Lin, V. P. Dravid, J. B. Ketterson, and R. P. H. Chang, Growth and characterization of buckybundles, *Appl. Phys. Lett.* 62, 1881 (1993).
51. X. K. Wang, R. P. H. Chang, A. Patashinski, and J. B. Ketterson, Magnetic susceptibility of buckytubes, *J. Mater. Res.* 9, 1578 (1994).
52. J. Heremans, C. H. Oik, and D. T. Morelli, Magnetic susceptibility of carbon structures, *Phys. Rev. B* 49, 15122 (1994).
53. J.-P. Issi, L. Langer, J. Heremans, and C. H. Oik, Electronic properties of carbon nanotubes: experimental results, *Carbon* 33, 941 (1995).
54. A. P. Ramirez, R. C. Haddon, O. Zhou, R. M. Fleming, J. Zhang, S. M. McClure, and R. E. Smalley, Magnetic susceptibility of molecular carbon: nanotubes and fullerite, *Science* 265, 84 (1994).
55. R. C. Haddon, Magnetism of the carbon allotropes, *Nature (London)* 378, 249 (1995).
56. A. S. Kotosonov, Texture and magnetic anisotropy of carbon nanotubes in cathode deposits obtained by the electric-arc method, *JETP Lett.* 70, 476 (1999).
57. O. Chauvet, L. Forro, W. Bacsa, D. Ugarte, B. Doudin, and W.A. de Heer, Magnetic anisotropies of aligned carbon nanotubes, *Phys. Rev. B* 52, R6963 (1995).
58. A. Fujiwara, F. Katayama, K. Tomiyama, H. Ootoshi, and H. Suematsu, Electronic transport and magnetic properties of carbon nanotubes, in *Molecular Nanostructures*, H. Kuzmany, J. Fink, M. Mehring, and S. Roth, Eds., World Scientific, Singapore (1998), pp. 439–442.

AU: Please provide article title.

59. F. Tsui, L. Jin, and O. Zhou, Anistropic magnetic susceptibility of multiwalled carbon nanotubes, *Appl. Phys. Lett.* 76, 1452 (2000).
60. P. de Rango, M. Lees, P. Lejay, A. Sulpice, R. Tournier, M. Ingold, P. Germi, and M. Pernet, Texturing of magnetic materials at high temperature by solidification in a magnetic field, *Nature (London)* 349, 770.
61. M. Fujiwara, N. Fukui, and Y. Tanimoto, Magnetic orientation of benzophenone crystals in fields up to 80.0 kOe, *J. Phys. Chem. B* 103, 2627 (1999).
62. T. Kimura, H. Ago, M. Tobita, S. Ohshima, M. Kyotani, and M. Yumura, Polymer composites of carbon nanotubes aligned by a magnetic field, *Adv. Mater.* 14, 1380 (2002).
63. M. Fujiwara, E. Oki, M. Hamada, Y. Tanimoto, I. Mukouda, and Y. Shimomura, Magnetic orientation and magnetic properties of a single carbon nanotube, *J. Phys. Chem. A* 105, 4383 (2001).
64. M. Fujiwara, K. Kawakami, and Y. Tanimoto, Magnetic orientation of carbon nanotubes at temperatures of 231 K and 314 K, *Mol. Phys.* 100, 1085 (2002).
65. D. A. Walters, M. J. Casavant, X. C. Qin, C. B. Huffman, P. J. Boul, L. M. Ericson, E. H. Haroz, M. J. O'Connell, K. Smith, D. T. Colbert, and R. E. Smalley, In-plane-aligned membranes of carbon nanotubes, *Chem. Phys. Lett.* 338, 14 (2001).
66. M. J. Casavant, D. A. Walters, J. J. Schmidt, and R. E. Smalley, Neat macroscopic membranes of aligned carbon nanotubes, *J. Appl. Phys.* 93, 2153 (2003).
67. S. Zaric, G. N. Ostojic, J. Kono, J. Shaver, V. C. Moore, M. S. Strano, R. H. Hauge, R. E. Smalley, and X. Wei, Estimation of magnetic susceptibility anisotropy of carbon nanotubes using magneto-photoluminescence, *Nano Lett.* 4, 2219 (2004).
68. M. J. O'Connell, S. M. Bachilo, C. B. Huffman, V. C. Moore, M. S. Strano, E. H. Haroz, K. L. Rialon, P. J. Boul, W. H. Noon, C. Kittrell, J. Ma, R. H. Hauge, R. B. Weisman, and R. E. Smalley, Band gap fluorescence from individual single-walled carbon nanotubes, *Science* 297, 593 (2002).
69. S. M. Bachilo, M. S. Strano, C. Kittrell, R. H. Hauge, R. E. Smalley, and R. B. Weisman, Structure-assigned optical spectra of single-walled carbon nanotubes, *Science* 298, 2361 (2002).
70. L. Langer, V. Bayot, E. Grivei, J.-P. Issi, J. P. Heremans, C. H. Oik, L. Stockman, C. van Haesendonck, and Y. Bruynseraede, Quantum transport in a multiwalled carbon nanotube, *Phys. Rev. Lett.* 76, 479 (1996).
71. J.-O. Lee, J.-R. Kim, J.-J. Kim, J. Kim, N. Kim, J.W. Park, K.-H. Yoo, and K.-H. Park, Magnetoresistance and differential conductance in multiwalled carbon nanotubes, *Phys. Rev. B* 61, R16362 (2000).
72. S. Roche and R. Saito, Magnetoresistance of carbon nanotubes: from molecular to mesoscopic fingerprints, *Phys. Rev. Lett.* 87, 246803 (2001).
73. G. Ferorov et al., Gate-dependent magnetoresistance phenomena in carbon nanotubes, *Phys. Rev. Lett.* (2005).

AU: Please provide volume and page numbers.